PHYSICAL REVIEW FLUIDS **3**, 064306 (2018)

Editors' Suggestion

Effects of particle size and density on dust dispersion behind a moving shock

Shuyue Lai
Department of Aerospace Engineering, University of Maryland, College Park, Maryland 20740, USA

Ryan W. Houim
Department of Mechanical & Aerospace Engineering, University of Florida, Gainesville, Florida 32611, USA and Department of Aerospace Engineering, University of Maryland, College Park, Maryland 20740, USA

Elaine S. Oran
Department of Aerospace Engineering, University of Maryland, College Park, Maryland 20740, USA

(Received 4 March 2018; published 26 June 2018; corrected 14 August 2018)

Numerical simulations are performed to study the effect of particle size and density on dust dispersion behind a moving shock. The numerical model used in this paper takes into account multiple particle types with a binning approach, and each bin of particles has its own characteristic uniform particle size and density. The model solves one set of governing equations for the gas phase and M sets of governing equations for the M particle types. Equations for each bin of particles are coupled with the gas flow as well as all other particle types. The specific conditions simulate a Mach-1.4 shock passing over a dust layer containing two uniformly mixed particle types. The background gas condition is at 67 kPa and 295 K. The dust layer is 1.27 cm thick and consists of spherical particles with selected sizes and densities. Preliminary one-dimensional computations of a shock passing through a dilute particle curtain containing different particle types suggest that particles with different sizes or densities behave differently and can separate into different clouds. Particles with larger inertia require a longer relaxation time to the postshock condition. The two-dimensional calculations show that larger particles are lifted to a higher level than smaller particles. In regions near the shock front, larger particles experience a smaller drag force, pushing the particles into the dust layer, and a larger lifting force, pulling the particles into the air. In addition, lighter particles are lifted higher than heavier particles due to a smaller inertia. Particle size plays a significant role on dust dispersion, while particle density has only a minor effect.

DOI: 10.1103/PhysRevFluids.3.064306

I. INTRODUCTION

Dust dispersion induced by gas flow is encountered in many aspects of science and engineering. In certain cases, the dispersed dust particles can be a threat to the environment and to human lives. For example, the entrainment of coal particles during a coal mine explosion can result in a more dangerous secondary explosion [1,2]; the airborne dust particles during a helicopter brownout landing can obscure the pilot's vision [3]; and the migration of the sand dues in desert regions by the action of wind can accelerate the process of desertification [4]. Thus, a better understanding of the dust-lifting mechanism and the possible factors affecting the level of dust dispersion is essential information needed to control particle motions that can help reduce risks.

Dust entrainment in a coal mine explosion is a mode of dust dispersion that involves the interaction of a granular bed and a shock wave generated from an explosion. This paper focuses on the problem of dispersing a layer of dust particles behind a moving shock wave, in which the conditions are characteristic of what is found in a coal mine. In this situation, shock waves initiated by an initial explosion produce forces that can lift coal dust as the shock propagates over the dust layer. The dispersed coal dust, if ignited by the explosion, may lead to a more devastating secondary explosion.

One common method of limiting coal-dust dispersion is to apply inert rock dust on top of the surface of the coal dust. Then, during an explosion, the dispersed rock dust can mix with the coal dust and prevent flame propagation by acting as a thermal inhibitor or heat sink [5]. Understanding the motions of inert particles and how they keep coal particles from lifting into the background atmosphere is essential for determining the type and frequency of inert dust applied. Rock dust varies substantially from coal dust, both size and density. Therefore, the question addressed in this paper is the following: How do particle size and density affect dust dispersion?

II. BACKGROUND

There have been a number of previous experimental and computational studies of the effect of particle size and density on dust dispersion behind a moving shock. These studies, however, lead to contradictory conclusions, some of which have been pointed out by Ugarte *et al.* [6].

For example, experiments preformed by Suzuki and Adachi [7] showed that the dust-lifting height increases as the particle size decreases. In addition, they showed a delay between the passage of the shock and dust lifting. Similarly, the numerical studies by Zhu *et al.* [8] showed that particle density had little effect on the lifting, but particle size has a significant effect. Finer dust is lifted more efficiently by a shock wave [8].

As an apparent contradiction, the experimental results done by Hwang [2] showed that particles with a diameter of 200 μm were lifted twice as high as particles with a 5-μm diameter, which indicates that larger particles are lifted higher than smaller particles. The delay in particle lifting increased as the particle size increased. Similarly, the simulations by Boyi *et al.* [9] suggested that, due to the effect of the lift force, the height of dispersed dust increased with the particle size. The same conclusion was also make by Ugarte *et al.* [6] with numerical simulations.

These apparently contradictory observations could result from the inconsistency in time and length scales or controlled variables among different studies. For example, Ugarte *et al.* [6] explained that their simulations differ from Suzuki's experiments because the results were evaluated at different distances (length) and times after the shock passed. In Suzuki's experiments, the observations were made within the 40-cm range of shock propagation, and delay in particle lifting was observed directly behind the shock. The simulations done by Ugarte *et al.* [6] were performed after the shock passed 300 cm down the channel, and the lifting delay process played a much less significant role in dust lifting. In addition, Chowdhury [10] noted that the particles of different sizes used in Suzuki and Adachi [7]'s experiments were different materials with approximately the same density but different morphology [10]. The interactions among particles with different physical properties could bring uncertainties to the results obtained by Suzuki and Adachi [7].

The numerical simulations summarized above assumed that the dust is a medium consisting of identical spherical particles. The composition of a granular flow is, in reality, much more complicated. Granular materials are a collection of rigid, macroscopic particles with an interstitial fluid that can be a gas or a liquid. A more realistic dust cloud is composed of a large number of particles with different particle diameters, and particles can behave differently according to the specific particle type. For example, when you shake a jar of mixed nuts, the larger nuts will move to the top of the heap while the smaller ones will stay at the bottom. The nuts interact with each other by friction, which is largely dependent on their the size and shape [11]. Similarly, the dust layer in a coal mine consists of mainly rock- and coal-dust particles with a wide range of sizes. According to the Office of Mine Safety and Health Research (OMSHR), coal dust consists of particles ranging from 0.375 to 234.1 μm and rock dust consists of particles ranging from 0.375 to 282.1 μm [12]. Depending on the particle size and density, particles in a dust layer can behave differently when they interact with a shock wave. Therefore, a multiphase model that accounts for multiple particle types can be expected to give results different from those for a single particle type.

This paper discusses the effects of particle size and density on dust dispersion by performing both one-dimensional (1D) simulations of a shock passing through a particle mixture and two-dimensional (2D) simulations of a shock passing over a dust layer containing two uniformly mixed particle types. The model used in this paper is based on that of Houim and Oran [13] and is now extended to account for different particle types using a binning approach. This model solves the Euler equations for both the gas phase and multiple particle types. Particles in each bin have their own uniform particle size and diameter. The governing forces acting on each particle type will be evaluated to study how different types of particles are lifted to different levels.

III. PHYSICAL AND NUMERICAL MODEL

A. Governing equations

This model is an extension of Houim and Oran's work [13], that now allows different particle sizes and densities. This is done with a particle binning approach, in which each bin contains particles of the same size and density. As a result, each bin adds an additional set of governing equations and can have different properties. The governing equations for each bin are coupled with the gas phase as well as all of the other particle bins. The three governing equations for the gas phase are

$$\frac{\partial \alpha_g \rho_g}{\partial t} + \nabla \cdot (\alpha_g \rho_g \boldsymbol{v}_g) = 0, \tag{1}$$

$$\frac{\partial \alpha_g \rho_g \boldsymbol{v}_g}{\partial t} + \nabla \cdot (\alpha_g \rho_g \boldsymbol{v}_g \boldsymbol{v}_g) + \nabla \alpha_g p_g = p_{\mathrm{int}} \nabla \alpha_g + \alpha_g \rho_g \boldsymbol{g} + \sum_{m=1}^{M} \{\boldsymbol{f}_{\mathrm{Drag,gm}} + \boldsymbol{f}_{\mathrm{Lift,gm}}\}, \tag{2}$$

$$\begin{aligned} &\frac{\partial \alpha_g \rho_g E_g}{\partial t} + \nabla \cdot [\alpha_g \boldsymbol{v}_g (\rho_g E_g + p_g)] \\ &\quad = -p_{\mathrm{int}} \sum_{m=1}^{M} \nabla \cdot (\alpha_{s,m} \boldsymbol{v}_{s,m}) + \alpha_g \rho_g \boldsymbol{g} \cdot \boldsymbol{v}_g + \sum_{m=1}^{M} \{(\boldsymbol{f}_{\mathrm{Drag,gm}} + \boldsymbol{f}_{\mathrm{Lift,gm}}) \cdot \boldsymbol{v}_g - q_{\mathrm{conv,gm}} \\ &\qquad + \phi_{\mathrm{visc,gm}} - \phi_{\mathrm{slip,gm}}\}. \end{aligned} \tag{3}$$

The four governing equations for particle type l are

$$\frac{\partial \alpha_{s,l} \rho_{s,l}}{\partial t} + \nabla \cdot (\alpha_{s,l} \rho_{s,l} \boldsymbol{v}_{s,l}) = 0, \tag{4}$$

$$\begin{aligned} &\frac{\partial \alpha_{s,l} \rho_{s,l} \boldsymbol{v}_{s,l}}{\partial t} + \nabla \cdot (\alpha_{s,l} \rho_{s,l} \boldsymbol{v}_{s,l} \boldsymbol{v}_{s,l}) + \nabla p_{sl,\mathrm{tot}} \\ &\quad = -\alpha_{s,l} \nabla p_g + \alpha_{s,l} \rho_{s,l} \boldsymbol{g} - \boldsymbol{f}_{\mathrm{Drag,gl}} - \boldsymbol{f}_{\mathrm{Lift,gl}} - \sum_{\substack{m=1 \\ m \neq l}}^{M} \{\boldsymbol{f}_{\mathrm{Drag,lm}}\}, \end{aligned} \tag{5}$$

$$\frac{\partial \alpha_{s,l} \rho_s E_{s,l}}{\partial t} + \nabla \cdot (\alpha_{s,l} \rho_{s,l} E_{s,l} \boldsymbol{v}_{s,l}) = -p_{s,l} \nabla \cdot \boldsymbol{v}_{s,l} - \dot{\gamma}_l - \phi_{\mathrm{visc}_g l} + \phi_{\mathrm{slip}_g l}, \tag{6}$$

$$\frac{\partial \alpha_{s,l} \rho_{s,l} e_{s,l}}{\partial t} + \nabla \cdot (\alpha_{s,l} \rho_{s,l} e_{s,l} \boldsymbol{v}_{s,l}) = q_{\mathrm{conv,gl}} + \dot{\gamma}_l. \tag{7}$$

Here, α, ρ, $\boldsymbol{v}$, and p represent the volume fraction, density, velocity, and pressure of the gas or particle phase, indicated by a subscript g or s. The subscripts l and m indicate the lth and the mth particle types, respectively. Also, E_g is the gas-phase total energy, e_s is the internal energy for the particle phase, and E_s represents the pseudothermal energy (PTE). The pressure at the gas-particle interface, p_{int}, is assumed to be the gas pressure p_g. In this model, the granular energy exchange between different particle bins, the dissipation of granular energy due to inelastic collisions between different particle bins, and the granular viscous stress terms are neglected. These terms are considered to be of secondary importance to the qualitative shock-dust structure and do not produce significant effects on the height of the dispersed dust layer, which is the major concern in our project. In addition, we neglect any phase changes between the gas and all of the particle types for simplicity. Some of the assumptions and the sensitivity of results to the model will be addressed in Sec. VII D.

The gas-phase total energy, E_g, is defined by

$$E_g = \frac{p_g}{\rho_g(\gamma - 1)} + \frac{1}{2}\boldsymbol{v}_g \cdot \boldsymbol{v}_g. \tag{8}$$

The particle-phase energy has been divided into two parts: the internal energy ($e_{s,l}$) and the PTE, which represents the energy due to random translational motion of particles [13].

The internal energy for particle type l, $e_{s,l}$, is determined by [13]

$$e_{s,l} = \int_{T_{\mathrm{ref}}}^{T} C_{v,sl}\, ds + e_{\mathrm{ref},l}, \tag{9}$$

where the specific heat capacity for the particle phase ($C_{v,sl}$) is constant and the energy at the reference temperature ($e_{\mathrm{ref},l}$) is zero. PTE is directly related to the granular temperature, $\theta_{s,l}$, using the following expression:

$$E_{s,l} = \tfrac{3}{2}\theta_{s,l}. \tag{10}$$

The granular temperature is a measure of the mean square of the particle velocity fluctuations, and represents the fluctuations of solid particles due to collisions.

The heat exchange between particle type m and gas phase, $q_{\mathrm{conv}_{gm}}$, is defined as a function of temperature difference,

$$q_{\mathrm{conv}_{g}m} = h_{\mathrm{mg}}(T_g - T_{s,m}), \tag{11}$$

where the heat exchange coefficient h_{mg} is defined as

$$h_{\mathrm{mg}} = 6\frac{\alpha_{s,m}\lambda_g \mathrm{Nu}_m}{d_{s,m}^2}. \tag{12}$$

The Nusselt number, Nu_m, is estimated using the work by Gunn [14],

$$\mathrm{Nu}_m = \left(7 - 10\alpha_g + 5\alpha_g^2\right)\left(1 + 0.7\mathrm{Re}_m^{0.2}\mathrm{Pr}_g^{1/3}\right) + \left(1.33 - 2.4\alpha_g + 1.2\alpha_g^2\right)\mathrm{Re}_m^{0.7}\mathrm{Pr}_g^{1/3}, \tag{13}$$

where

$$\alpha_g = 1 - \sum_{l=1}^{M}\alpha_{s,l}. \tag{14}$$

Here Pr_g is the gas phase Prandtl number, and λ_g is the gas phase thermal conductivity. The Reynolds number related to particle type m is

$$\mathrm{Re}_m = \frac{\rho_g|\boldsymbol{v}_{s,m} - \boldsymbol{v}_g|d_{s,m}}{\mu_g}. \tag{15}$$

The transfer of PTE to kinetic energy is represented by $\phi_{\mathrm{visc}_{gm}}$, the viscous damping [15],

$$\phi_{\mathrm{visc}_{g}m} = 3K_{\mathrm{mg}}\theta_{s,m}. \tag{16}$$

The PTE production due to slip between gas and particle type m is [16]

$$\phi_{\mathrm{slip}_{g}m} = \frac{81\alpha_{s,m}\mu_g^2}{g_0 d_{s,m}^3 \rho_{s,m}\sqrt{\pi}}\frac{\rho_s\theta_{s,m}^{3/2}}{d_{s,m}}. \tag{17}$$

The dissipation of PTE due to collisions between particles is given by Lun *et al.* [17],

$$\dot{\gamma}_l = \frac{12(1 - e^2)g_{0,ll}\alpha_{s,l}^2}{\sqrt{\pi}}\frac{\rho_{s,l}\theta_{s,l}^{3/2}}{d_{s,l}}. \tag{18}$$

The radial distribution function between particle type l and m, $g_{0,lm}$, represents the probability of collisions between the two particle types when the granular phase becomes dense. For a mixture of hard spheres, the equation is [18]

$$g_{0,lm} = \frac{1}{\alpha_g} + \frac{3d_l d_m}{\alpha_g^2(d_l + d_m)} \sum_{q=1}^{M} \frac{\alpha_q}{d_q}, \tag{19}$$

where d_l and d_m are the particle diameters for type l and type m, respectively.

For monosized particles, the maximum packing limit for spherical particles are 0.65. For particles containing multiple sizes, the packing limit varies and the correlation developed by Yu and Standish is being used [19,20]:

$$\alpha_{s,\mathrm{mix}}^{\max} = \min\left\{ \frac{\alpha_{s,i}^{\max}}{1 - \sum_{j=1}^{i-1}\left(1 - \frac{\alpha_{s,i}^{\max}}{pi,j}\frac{cx_i}{X_{ij}}\right) - \sum_{j=i+1}^{M} \frac{\alpha_{s,i}^{\max}}{pi,j}\frac{cx_i}{X_{ij}}} \right\}, \quad i = 1,2,\ldots,M, \tag{20}$$

where

$$cx_i = \frac{\alpha_{s,i}}{\sum_{j=1}^{M} \alpha_{s,j}}, \tag{21}$$

$$X_{i,j} = \begin{cases} \frac{1-r_{ij}^2}{2-\alpha_{s,i}^{\max}} & \text{if } j < i \\ 1 - \frac{1-r_{ij}^2}{2-\alpha_{s,i}^{\max}} & \text{if } j \geqslant i, \end{cases} \tag{22}$$

$$p_{ij} = \begin{cases} \alpha_{s,i}^{\max} + \alpha_{s,i}^{\max}\left(1 - \alpha_{s,i}^{\max}\right)\left(1 - 2.35 r_{ij} + 1.35 r_{ij}^2\right) & \text{if } r_{ij} < 0.741 \\ \alpha_{s,i}^{\max} & \text{if } r_{ij} \geqslant 0.741, \end{cases} \tag{23}$$

and

$$r_{ij} = \begin{cases} \frac{d_{p,i}}{d_{p,j}} & \text{if } i \geqslant j \\ \frac{d_{p,j}}{d_{p,i}} & \text{if } i < j. \end{cases} \tag{24}$$

Here $\alpha_{s,i}^{\max}$ is the maximum packing limit of individual particle type i and is assumed to be 0.65.

In this model, a “mixture granular temperature” is defined by [18]

$$\Theta_{s,\mathrm{mix}} = \frac{\sum_{m=1}^{M} \alpha_{s,m}\rho_{s,m}\Theta_{s,m}}{\sum_{m=1}^{M} \alpha_{s,m}\rho_{s,m}}. \tag{25}$$

This mixture value is only used to calculate the granular compaction wave speed ($c_{s,\mathrm{mix}}$), which is assumed to be the same for all particle types in a computational cell. The compaction wave speed for the granular mixture can be written as [13]

$$c_{s,\mathrm{mix}}^2 = \frac{1}{\rho_{\mathrm{mix}}}\left[\left.\frac{\partial(P_{s,\mathrm{mix}} + P_{\mathrm{fric,mix}})}{\partial\alpha_{\mathrm{mix}}}\right|_{\Theta_{\mathrm{mix}}} + \frac{2}{3}\frac{\Theta_{\mathrm{mix}}\left(\frac{\partial P_{\mathrm{mix}}}{\Theta_{\mathrm{mix}}}\Big|_{\alpha_{\mathrm{mix}}}\right)^2}{\rho_{\mathrm{mix}}\alpha_{\mathrm{mix}}^2} \right], \tag{26}$$

and this leads to

$$c_{s,\mathrm{mix}}^2 = \theta_{s,\mathrm{mix}}\left(A + \tfrac{2}{3}A^2 + \alpha_{s,\mathrm{mix}}B\right) + c_{\mathrm{fric,mix}}^2, \tag{27}$$

where

$$A = 1 + 2(1+e)\alpha_{\mathrm{mix}}g_{0,\mathrm{mix}}, \tag{28}$$

$$B = 2(1+e)(g_{0,\mathrm{mix}} + \alpha_{\mathrm{mix}}g'_{0,\mathrm{mix}}), \tag{29}$$

and

$$g'_{0,\text{mix}} = \frac{g_{0,\text{mix}}^2}{3\alpha_{s,\max}}\left(\frac{\alpha_{s,\max}}{\alpha_{s,\text{mix}}}\right)^{2/3}. \tag{30}$$

Here

$$\alpha_{s,\text{mix}} = \sum_{m=1}^{M} \alpha_{s,m}, \tag{31}$$

$$\rho_{\text{mix}} = \frac{\sum_{m=1}^{M} \alpha_{s,m}\rho_{s,m}}{\alpha_{s,\text{mix}}}, \tag{32}$$

and

$$\frac{1}{g_{0,\text{mix}}} = 1 - \left(\frac{\alpha_{s,\text{mix}}}{\alpha_{s,\max}}\right)^{1/3}. \tag{33}$$

The momentum-exchange equation for particle type l is a function of the drag, lift, Archimedes force, intergranular stress, and particle-hindrance force. The equations involved in calculating these forces will be discussed separately in the following section.

1. Archimedes force

The term $-\alpha_{s,l}\nabla p_g$ in the particle-phase momentum equation is called the Archimedes force, which is the result of gas-phase pressure pushing particle type l.

2. Intergranular stress

The quantity $p_{sl,\text{tot}}$ is the total intergranular stress, which is defined as the sum of the solids pressure and the frictional pressure,

$$p_{sl,\text{tot}} = p_{s,l} + p_{\text{fric},l}. \tag{34}$$

The solids pressure $p_{s,l}$ takes into account the collisional effect of the particles and is defined as [21]

$$P_{s,l} = \alpha_{s,l}\rho_{s,l}\Theta_{s,l} + \sum_{m=1}^{M} P_{c,lm}. \tag{35}$$

Here $P_{c,lm}$ is the collisional part of the pressure between particle types l and m, and $\alpha_{s,l}\rho_{s,l}\Theta_{s,l}$ is the kinetic term for particle type l. $P_{c,lm}$ is defined as [21]

$$P_{c,lm} = \frac{\pi(1+e)d_{lm}^3 g_{0,lm} n_l n_m m_l m_m m_0 \theta_l \theta_m}{3\left(m_l^2\theta_l + m_m^2\theta_m\right)}\left[\frac{m_0^2\theta_l\theta_m}{\left(m_l^2\theta_l + m_m^2\theta_m\right)(\theta_l+\theta_m)}\right]^{3/2} \times (1 - 3\Delta + 6\Delta^2 - 10\Delta^3), \tag{36}$$

where e is the coefficient of restitution and is related to the elasticity of the collisions [15]. The quantity m_l is the mass of a particle and n_l is the number of particles. For spherical particles,

$$m_l = \frac{\pi}{6}d_l^3\rho_l, \tag{37}$$

$$n_l = \frac{6\alpha_l}{\pi d_l^3}, \tag{38}$$

$$d_{lm} = \frac{d_l + d_m}{2}, \tag{39}$$

$$m_0 = (m_l + m_m), \tag{40}$$

and

$$\Delta = \frac{m_l\theta_l - m_m\theta_m}{\left[\left(m_l^2\theta_l^2 + m_m^2\theta_m^2\right) + \theta_l\theta_m\left(m_l^2 + m_m^2\right)\right]^{1/2}}. \tag{41}$$

The total intergranular stress is defined as the sum of the solids and friction pressure for each particle type,

$$P_{sl,\mathrm{tot}} = P_{s,l} + P_{\mathrm{fric},l}. \tag{42}$$

The frictional pressure for particle type l, $P_{\mathrm{fric},l}$, represents the effect of friction between particles, and this is essential for preventing the particle phase in dense region from packing to an unphysically high level [13]. The relation used here was developed by Johnson and Jackson [22] and now modified based on the law of partial pressure from kinetic theory,

$$P_{\mathrm{fric},l} = \begin{cases} 0 & \text{if } \alpha_{s,\mathrm{tot}} < \alpha_{s,\mathrm{crit}} \\ 0.1\frac{(\alpha_{s,\mathrm{tot}}-\alpha_{s,\mathrm{crit}})^2}{(\alpha_{s,\max}-\alpha_{s,\mathrm{tot}})^5}\alpha_{s,l} & \text{if } \alpha_{s,\mathrm{tot}} \geqslant \alpha_{s,\mathrm{crit}}, \end{cases} \tag{43}$$

where $\alpha_{s,\mathrm{crit}}$ is set to be a critical value of 0.5.

3. *Drag force*

The drag force between gas and particle type l is defined by the correlation of Gidaspow [15],

$$\boldsymbol{f}_{\mathrm{drag,gl}} = K_{l,g}(\boldsymbol{v}_{s,l} - \boldsymbol{v}_g), \tag{44}$$

where $K_{l,g}$ is the gas-solid exchange coefficient. The Gidaspow model is used again for $K_{l,g}$, which is a combination of the Wen and Yu model and the Ergun model [15,23,24],

$$K_{l,g} = \begin{cases} 0.75C_{d,l}\frac{\rho_g\alpha_g\alpha_{s,l}|\boldsymbol{v}_{s,l}-\boldsymbol{v}_g|}{d_{s,l}\alpha_g^{2.65}} & \text{if } \alpha_g \geqslant 0.8 \\ 150\frac{\alpha_{s,l}^2\mu_g}{\alpha_g d_{s,l}^2} + 1.75\frac{\rho_g\alpha_{s,l}|\boldsymbol{v}_{s,l}-\boldsymbol{v}_g|}{d_{s,l}} & \text{if } \alpha_g < 0.8. \end{cases} \tag{45}$$

Here the drag coefficient $C_{d,l}$ for particle type l is defined as

$$C_{d,l} = \begin{cases} 24(\alpha_g\mathrm{Re}_l)^{-1}[1 + 0.15(\alpha_g\mathrm{Re}_l)^{0.687}] & \text{if } \alpha_g\mathrm{Re} < 1000 \\ 0.44 & \text{if } \alpha_g\mathrm{Re} \geqslant 1000. \end{cases} \tag{46}$$

4. *Lift force*

The lift force f_{Lift} induced by particle type l acting on gas phase is modeled by the Magnus lift force [25],

$$\boldsymbol{f}_{\mathrm{Lift,l}} = C_l\alpha_{s,l}\rho_g(\boldsymbol{v}_{s,l} - \boldsymbol{v}_g) \times (\nabla \times \boldsymbol{v}_g), \tag{47}$$

where C_l is the lift coefficient, which typically takes a value of 0.5.

5. *Particle-hindrance force*

The particle-hindrance force between particle types l and m is a draglike term between the two corresponding particle types and is defined as [15]

$$\boldsymbol{f}_{\mathrm{Drag,lm}} = K_{lm}(\boldsymbol{v}_l - \boldsymbol{v}_m). \tag{48}$$

The solid-solid exchange coefficient between particle types l and m is [26]

$$K_{lm} = \frac{3(1 + e_{lm})\left(\frac{\pi}{2} + C_{fr,lm}\frac{\pi^2}{8}\right)\alpha_l\rho_l\alpha_m\rho_m(d_l + d_m)^2 g_{0,lm}}{2\pi\left(\rho_l d_l^3 + \rho_m d_m^3\right)}|\boldsymbol{v}_l - \boldsymbol{v}_m|, \tag{49}$$

where e_{lm} is the coefficient of restitution and $C_{fr,lm}$ is the coefficient of friction between particle types l and m. The friction between different particle types is neglected in the simulation ($C_{fr,lm} = 0$).

TABLE I. Forces acting on particle type l.

Channel height	H	20 cm
Channel length	L	300 cm
Background temperature	T_0	295 K
Background pressure	P_0	67 kPa
Shock Mach number	M_s	1.4
Initial dust-layer height	h_d	1.27 cm
Particle volume fraction (type I)	$\alpha_{s,1}$	0.235
Particle volume fraction (type II)	$\alpha_{s,2}$	0.235

B. Numerical algorithms

A detailed description of the numerical algorithm can be found in Houim and Oran [13]. The Strang operator-splitting algorithm is used to divide the governing equations into two parts: the hyperbolic terms and the source terms. The hyperbolic terms are solved using a high-order Godunov-based scheme [27], where the primitive variables are implemented using a MUSCL (Monotonic Upwind Scheme for Conservation Laws) method with a third-order parabolic reconstruction. An adaptive total variation diminishing (TVD) scheme with minmod slope limiter is also adopted to reduce small oscillations near discontinuities. A modified HLLC (Harten-Lax-van Leer-Contact) method, which returns primitive variables directly, is used to solve for the gas-phase flux. The granular flux is computed using a modified AUSM (Advection Upstream Splitting Method)$^+$-up method to increase dissipation in highly packed regions [27]. The lifting Magnus force is discretized using a first-order backward differencing scheme. The Strang operator [13] further splits the source terms into two parts: (1) drag, particle-hindrance effect, and convective heat transfer and (2) pseudothermal energy production and dissipation. These source terms are integrated analytically into the solutions [28] and the details of the expressions can be found in Houim and Oran [13]. The solution algorithm uses a third-order Runge-Kutta scheme [29] for time advancement. Adaptive mesh refinement is implemented through the Boxlib library [30].

IV. EVALUATION OF FORCES

We can identify six forces acting on particles. Evaluating these forces helps to explain how the particle size and density affect dust dispersion. Table I summarizes the six controlling forces that act on particle type l. The lift and drag forces result from the velocity difference between the particles and the gas. The Archimedes force is due to the gas-phase pressure pushing on the particles. The intergranular stress corresponds to the collisional and frictional effect of the particles. The particle-hindrance force is a draglike force between the two particle types. Gravity is not important in the timescale of the simulations, so it is exempted from the discussion. Now, we only focus on the equations of forces that are related to d_s and ρ_s.

The collisional part of the intergranular stress (p_s) used in expression (2) in Table I depends on the particle density. A greater particle density results in a larger intergranular stress [$\nabla p_s \propto \rho_s$; see Eq. (35)].

The momentum exchange coefficient between particle type l and the gas (K_{lg}) used in expression (3) in Table I for the drag force is inversely proportional to the particle diameter. In addition, it is also proportional to the the drag coefficient [C_d; see Eq. (45)], which is inversely related to the relative velocity and the particle diameter. In other words, a larger particle diameter results in a smaller drag force.

The solid-solid exchange coefficient ($K_{s,lm}$) between particle types l and m used in expression (5) in Table I for the particle-hindrance force depends on the particle size and density for both type l and m particles. Similar to the gas-phase drag force, it accelerates slower particles while decelerating faster particles.

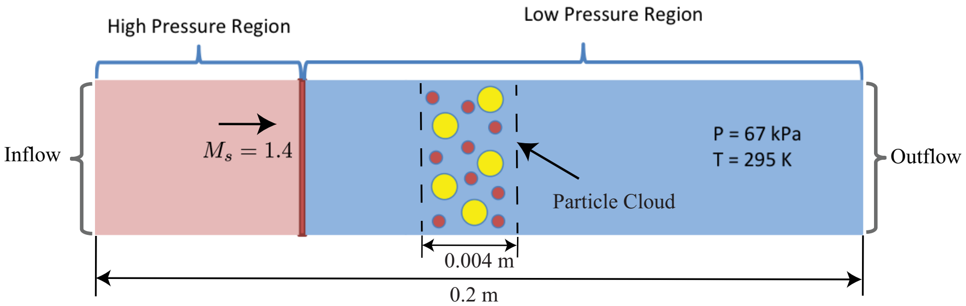

FIG. 1. Initial conditions for a one-dimensional test of a shock moving through a particle cloud containing two uniformly mixed particle types.

The lift force, Archimedes force, and gravity are independent of the particle size and density. Nevertheless, all governing forces are coupled with each other, and so they may also be affected by particle size and density. For example, the lift force [expression (4) in Table I], which produces positive acceleration for most of the dispersed dust [6], is modeled by the Magnus force. The lifting force along vertical direction is proportional to the velocity difference between the particle phase and gas phase along horizontal direction,

$$f_{Lift,y} = C_l \alpha_s \rho_g (u_s - u_g)\left(\frac{\partial v_g}{\partial x} - \frac{\partial u_g}{\partial y}\right). \tag{50}$$

V. ONE-DIMENSIONAL SHOCK-PARTICLE INTERACTION

Here, one-dimensional tests of a shock wave interacting with a cloud of particle mixture containing two or more types of particles are presented to show how different types of particles behave with the interaction to a shock wave.

The initial setup for the base case is illustrated in Fig. 1. A Mach-1.4 shock driven by the high-pressure gas is moving to the right and passes through a particle mixture. The right section (blue) is the low-pressure region and is 67 kPa and 295 K. (The value of 67 kPa was chosen for consistency with the work of Ugarte *et al.* [6].) The left section (red) represents the postshock condition. The particle cloud consists of two different types of particles. This test models a scenario in which a shock wave from an explosion interacts with a dilute dispersed dust clouds containing coal and inert rock particles. The initial volume fraction of each type of particle is 0.026% (based on an explosive coal-air burning condition).

A. Results with two particle bins

Here, two particle types are considered (same setup as in Fig. 1). Separate simulations were used to study the effects of varying particle size and density. The input parameters for the particle types are summarized in Table II. The sizes and densities selected are within the range for coal- and rock-dust particles.

1. Effect of particle size

The profiles in Fig. 2 show how the system evolves when the two particle densities are the same, but their sizes are different (case I). The vertical dashed lines in Fig. 2(a) indicate the location of the gas shock. As the shock wave moves through the particle cloud, there is a small peak in the concentration of the smaller particles (see Fig. 2 at 17 μs), indicating that the smaller particles react faster to the propagating shock wave. In time, the different particle types are separated.

TABLE II. Input conditions of particle size and density.

		Diameter (d_s) [μm]	Density (ρ_s) [kg/m^3]
Case I	Particle I	80	1300
	Particle II	10	1300
Case II	Particle I	10	1300
	Particle II	10	2700

The velocity profile in Fig. 2(b) shows that the particles inside each of the separated clouds stays roughly the same, and this velocity increases with time. Smaller particles propagate with a higher velocity than larger particles through drag and other aerodynamic effects. The velocity differences cause the uniformly mixed particle cloud to segregate into two different clouds according to the particle size. At 100 μs, a separation between the two particle types is already apparent. At 200 μs, the two particle types are completely separated.

2. Effect of particle density

Figure 3 shows how the system evolves when the two particle sizes are the same, but their densities are different (case II). Similarly, the two particle clouds separate into different regions according to different densities. The velocity profiles show that heavier particles are accelerated more slowly than the lighter particles. The two types of particles propagate with different velocities and the separation process increases with time. This separation is slower than that for the previous case (same density but different sizes). At 200 μs, the two types of particles are not completely separated.

With the two simulations shown above, we find that particles with different size or density can separate from each other even when they were initially uniformed mixed with each other. Modeling

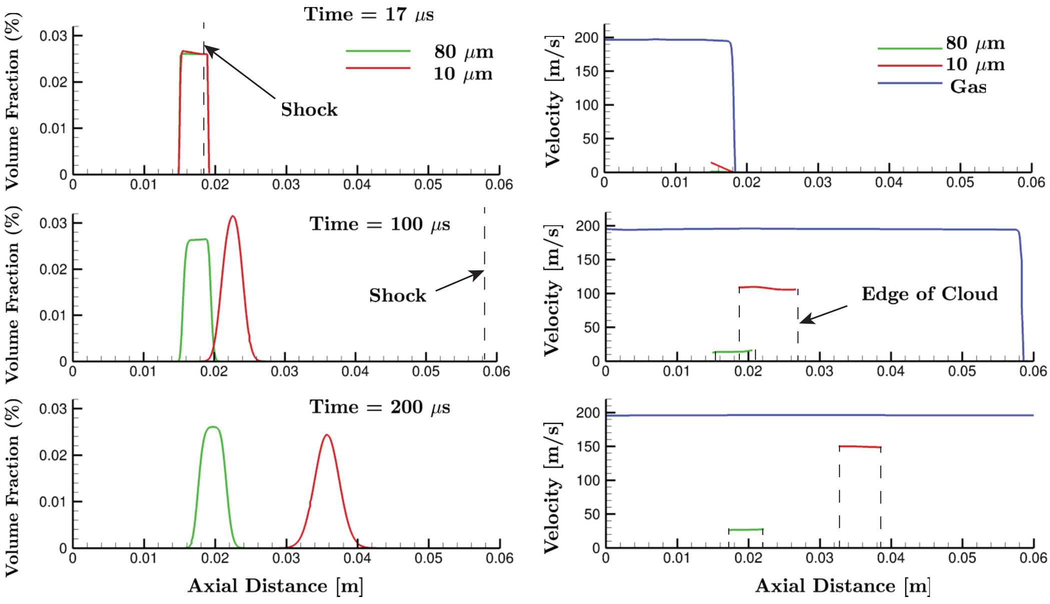

(a) (b)

FIG. 2. Computed (a) volume fractions for the two particle types ($d_{s1} = 80\,\mu$m, $d_{s2} = 10\,\mu$m) and (b) gas and particle velocities at 17, 100, and 200 μs. The edge of the partice cloud is defined by a volume fraction of 5×10^{-5}.

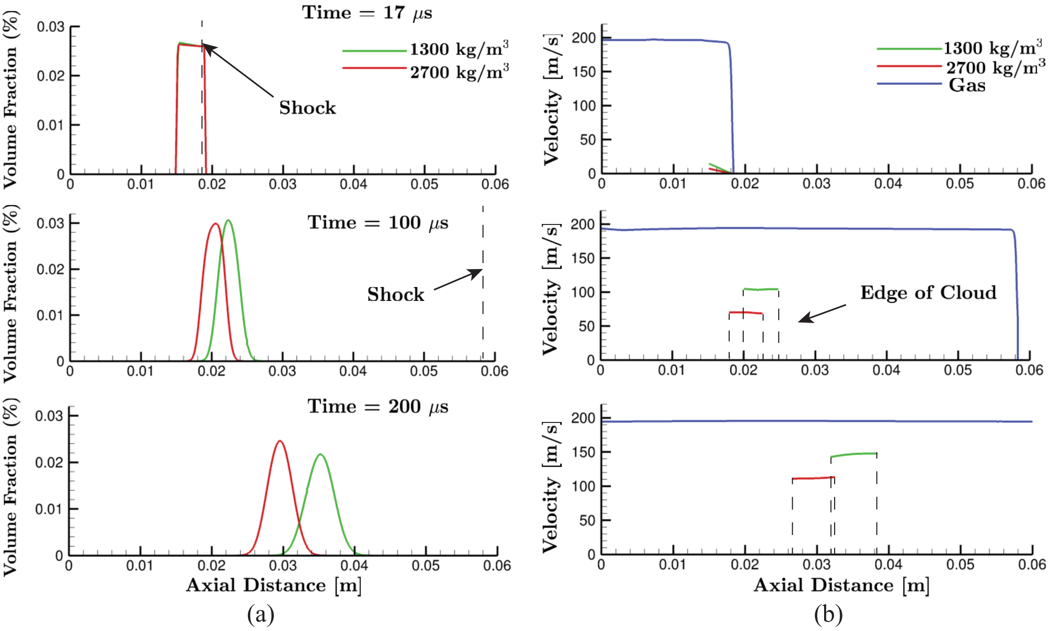

FIG. 3. Computed (a) volume fractions for the two particle types ($\rho_{s1} = 1300\,\mathrm{kg/m^3}$, $\rho_{s2} = 2700\,\mathrm{kg/m^3}$) and (b) gas and particle velocities at 17, 100, and 200 μs. The edge of the particle cloud is defined by a volume fraction of 5×10^{-5}. Dashed lines indicate the locations of the gas shock and the edge of the dust clouds.

the dust particles with only one particle bin (i.e., uniform size and density) fails to capture the separation process. The reason why the separation process occurs between different particle types will be discussed later.

B. Results with six particle bins

In a coal mine, both coal and rock particles are present in a range of sizes. Here, however, we assume a uniform diameter for the coal particles while dividing the rock dust into five particle bins, where each bin is characterized by a different particle size, but they all have the same density. The division is based on the OMSHR's reference size distribution chart [12]. The five types of rock-dust particles have approximately the same volume fraction and the overall volume fraction for the rock particles is 0.026%. The diameters and volume fractions for the five types of rock-dust particles are listed in Table III. The coal dust has a density of 1300 kg/m^3 and a diameter of 10 μm. All rock-dust particles have a density of 2700 kg/m^3. The initial volume fraction for the coal-dust particles is set to be 0.026%.

TABLE III. Rock-dust size distribution.

Size range [μm]	Averaged diameter ($d_{s,i}$) [μm]	Volume fraction ($\alpha_{s,i}$) [%]
0 – 5.61	1.685	0.00511
5.61 – 15.65	8.931	0.00546
15.65 – 52.62	26.201	0.00510
52.62 – 121.83	81.633	0.00555
121.83 – 339.90	171.239	0.00478

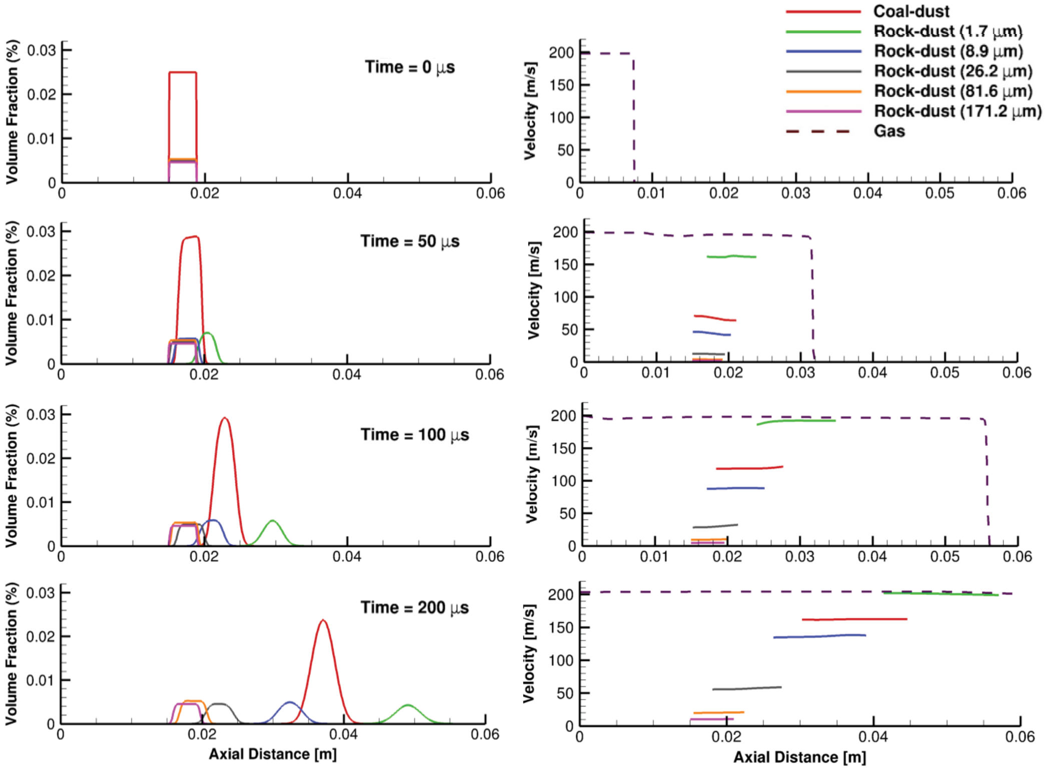

(a) Particle Volume Fraction

(b) Velocity

FIG. 4. Computated (a) coal- and rock-dust volume fraction and (b) gas and particle velocities at 0, 50, 100, and 200 μs. The edge of the cloud in panel (b) is defined by a volume fraction of 10^{-9}.

The computed results are shown in Fig. 4. Similar to the results with two particle bins, the uniformly mixed cloud separates into different dust clouds. The particles with a smaller size and density are accelerated faster by the postshock gas condition than particles with a larger size and density. The 1.7-μm rock dust (green) has the highest velocity (approaching the gas-phase velocity) and is completely separated from all the other particle bins by 200 μs. The 171.2-μm rock dust travels with the slowest velocity and lags behind all other particle types. The velocity of the coal particles (red) is lower than the 1.7-μm rock particles, but larger than the other rock-dust particles.

C. Discussion

1. *Effect of particle size and density*

In case I, where the two types of particles have the same density but different sizes, larger particles are accelerated more slowly than smaller particles. Figure 5 shows the average velocity of the two types of particles and the postshock gas velocity as a function of time. At 200 μs, the smaller particles have a velocity of 150 m/s, while the larger particles have a velocity of only 30 m/s. From an evaluation of the forces in Table I, the dominant force acting on the particles is the drag force, which is inversely proportional to the particle size and proportional to the velocity difference between gas and the particles [$\propto (\boldsymbol{v}_g - \boldsymbol{v}_{s,l})$]. For each particle type, the acceleration due to drag decreases with time due to a reduction in the velocity difference between the gas and particle velocity. Smaller particles experience a larger acceleration due to drag force and so accelerate much faster than the larger particles. The larger particles, on the other hand, have greater inertia and relax slowly to the

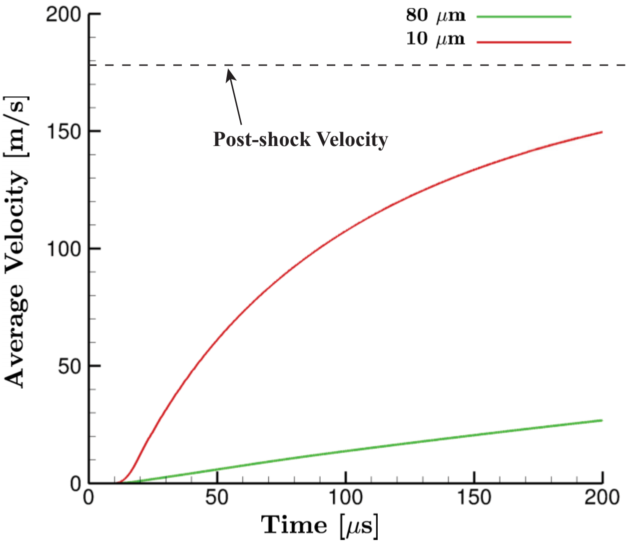

FIG. 5. Average velocities for both types of particles in case I ($d_s = 10$, $80\,\mu$m; $\rho_{s1} = \rho_{s2} = 1300$ kg/m^3) as a function of time in the postshock flow.

postshock condition. Drag forces in the postshock flow accelerate different particles at different rates. This, in turn, causes the uniformly fixed particle cloud to segregate into two different clouds. Here, the particle-hindrance effect is too small to reduce the velocity difference between the larger and the smaller particles.

For the simulation where the two particle bins have the same size but different densities, the drag forces acting on the two types of particles are similar, since the drag force is independent of particle density. The accelerations due to the drag force, however, are different for the two types of particles. Heavier particles have smaller accelerations due to drag than lighter particles since they have a greater inertia. Therefore, heavier particles propagate with a lower velocity than lighter particles, and this velocity difference causes the separation to occur.

2. *Modeling multiple particle types*

The separation process in the simulations shown above indicates the necessity of modeling multiple particle types, since this effect cannot be captured using a single-sized particle model. Dividing the particles into different particle types leads to more accurate results when the particle size or density in the dust varies greatly.

This is especially important in 2D simulations of the dust-lifting process in an underground coal mine, where the particle size and density are crucial for applying inert rock dust to reduce the coal-dust dispersion behind a moving shock wave. Similar to the 1D separation process, the rock and coal particles are expected to be lifted to different heights according to their sizes and densities. Therefore, dividing the particles into different types is essential in studying how the inert particles affect the motion of coal particles.

Increasing the number of particle types increases the realism of the computations, but it also increases the computational expense. The total number of equations in a one-dimensional, single-gas-phase, nonreactive calculation involving N particle types is

$$N_{eq} = 3 + 4N_{\text{bin}}, \tag{51}$$

where N_{eq} is the number of equations involved and N_{bin} is the number of particle bins. For a calculation involving 6 particle bins, 27 equations are needed, and this can be even more computationally

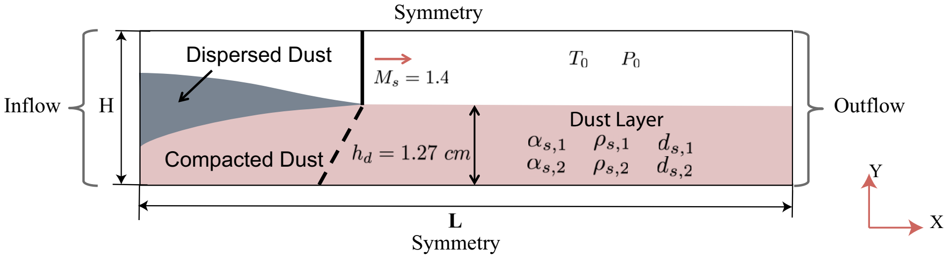

FIG. 6. Initial setups for two-dimensional simulations. The layer contains two particle types that are uniformly mixed with each other.

expensive for a two-dimensional calculation. There is, therefore, a tradeoff between the level of realism and accuracy of the simulation and the computational cost.

VI. TWO-DIMENSIONAL DUST DISPERSION

This section presents two-dimensional simulations of a shock passing over a dust layer. The setup for the simulations is shown in Fig. 6. Initially, a layer of dust containing two uniformly mixed particle types is placed on the bottom of a channel. A shock wave of Mach 1.4 is moving from the left to the right. The dust-layer thickness (h_d) is 1.27 cm and the initial particle volume fractions for both particle types are set to be identical ($\alpha_{s1} = \alpha_{s2} = 0.235$). The background pressure (P_0) and temperature (T_0) are 67 kPa and 295K, respectively. The left and right sides of the channel are nonreflecting, inflow-outflow boundary conditions and the top and bottom sides of the domain are symmetry planes. (These initial conditions are based on the experiments performed by Chowdhury *et al.* [31].) The input parameters are shown in Table IV.

A. Effect of particle size

Two test cases are performed to study the effect of particle size on dust dispersion. The size and density of the two types of particles are shown in Table V. The particle density is assumed to be 1300 kg/m^3 and remain fixed. Particle type I is assumed to be the larger particles in both cases.

Figure 7 shows the particle volume fraction for both particle types in the two test cases. The isobar of $P = 67$ kPa indicates the location of the gas shock. Figure 8 shows the edge of the dispersed dust (defined as $\alpha_s = 5 \times 10^{-5}$) with respect to the initial dust-layer height as a function of distance behind the shock wave. For each case, the larger-diameter particles [Figs. 7(a) and 7(c)] are lifted significantly higher than the particles with smaller diameters [Figs. 7(b) and 7(d)]. The smaller particles are lifted only a small amount. As we increase the size of type I particles from 80 μm (case I) to 120 μm (case II), the heavier 120-μm particles are lifted even higher, and more particles

TABLE IV. Initial parameters and geometrical condition for 2D simulations.

Channel height	H	20 cm
Channel length	L	300 cm
Background temperature	T_0	295 K
Background pressure	P_0	67 kPa
Shock Mach number	M_s	1.4
Initial dust-layer height	h_d	1.27 cm
Particle volume fraction (type I)	$\alpha_{s,1}$	0.235
Particle volume fraction (type II)	$\alpha_{s,2}$	0.235

TABLE V. Input conditions of particle size and density.

		Diameter (d_s) [μm]	Density (ρ_s) [kg/m^3]
Case I	Particle I	80	1300
	Particle II	10	1300
Case II	Particle I	120	1300
	Particle II	10	1300

are dispersed than the 80-μm particles. In general, the dust-lifting height depends strongly on the particle size. The reason for this and the related governing forces acting on different particle types will be addressed in the discussion section below.

B. Effect of particle density

Now consider simulations containing two particle types with identical particle size but different densities. Table VI summarizes the input parameters for the two particle types. Figure 9 shows the particle volume fraction for both particle types in the two test cases with the location of the gas shock indicated. Figure 10 shows the dust-lifting height as a function of distance behind the shock. These results indicate that the particle density has a minor effect on the dust-lifting height. In case I, the dust dispersion is very similar for the two types of particles. As the density of type II particles is increased from 1500 to 3000 kg/m^3 in case II, the difference becomes more obvious. Heavier particles (3000 kg/m^3) are lifted lower than the lighter particles (1000 kg/m^3). Comparing the dust-lifting height in both cases, type I particles (1000 kg/m^3) are lifted higher in case I than in case II, even though their size and density remain unchanged.

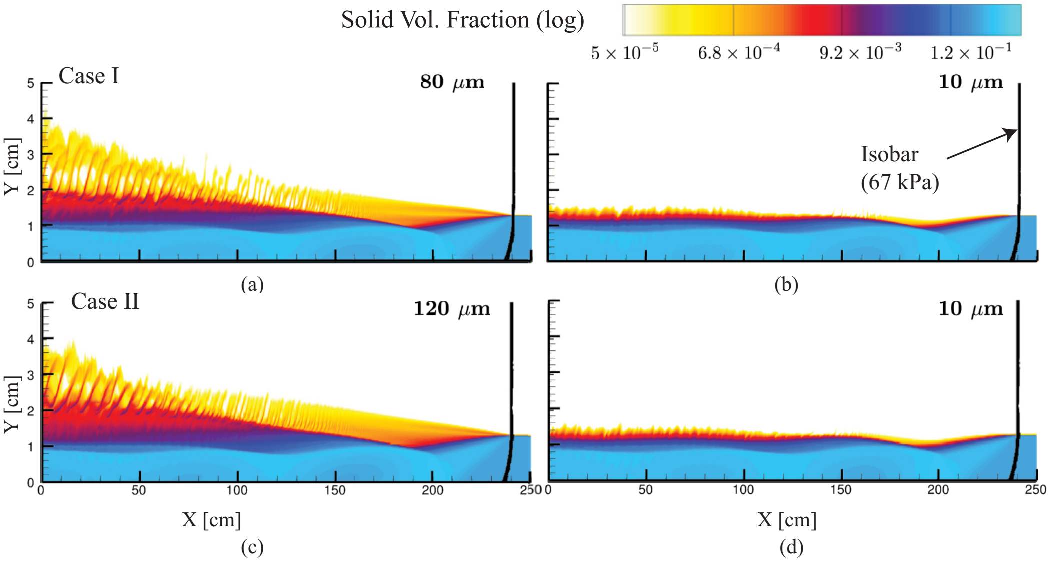

FIG. 7. Computed particle volume fractions for both particle types in cases I and II. (a) Particle I in case I ($d_s = 80$ μm); (b) particle II in case I ($d_s = 10$ μm); (c) particle I in case II ($d_s = 120$ μm); and (d) particle II in case II ($d_s = 10$ μm).

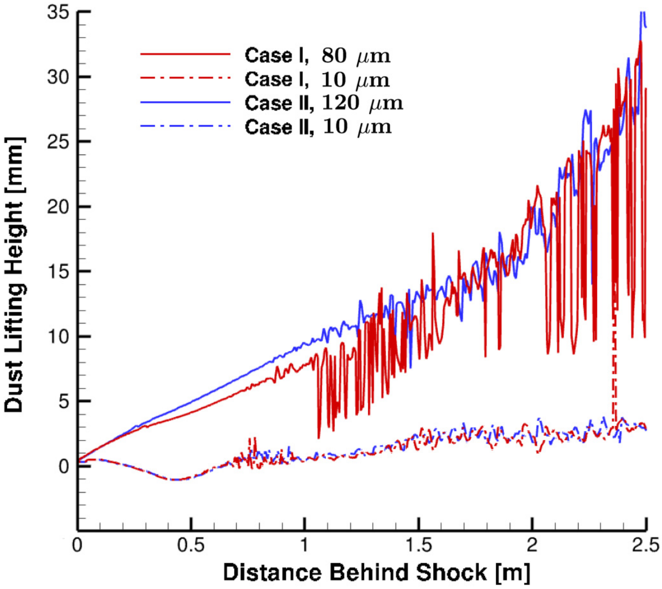

FIG. 8. Computed dust-lifting height for different particle diameters in both test cases. The edge of the dust layer is defined as $\alpha_s = 5 \times 10^{-5}$.

VII. DISCUSSIONS OF 2D SIMULATIONS

A. Effect of particle size

In the 2D calculations, larger particles are lifted higher than smaller particles. To understand why this occurs, the forces acting on both particle types are analyzed (Table I). Figure 11 shows the net accelerations as well as the accelerations due to drag, lift, Archimedes force, intergranular stress, and particle-hindrance force for both particle types ($d_{s,1} = 120\ \mu\text{m}$, $d_{s,2} = 10\ \mu\text{m}$, $\rho_{s,1} = \rho_{s,2} = 1300\ \text{kg/m}^3$) along the vertical direction.

According to Ugarte *et al.* [6], the gas shock curves and degenerates into a compression wave as it enters the dust layer. The compression wave compacts the particles in the layer and evolves into a granular compaction wave through particle collisional and frictional effects. The compaction wave reflects from the bottom of the channel and forms a reflected compaction wave. This reflected wave propagates upward and interacts with the surface of the dust layer, producing acoustic waves, which can enhance the flow oscillation [6]. The compaction wave and reflected compaction wave are marked in the intergranular stress contour in Fig. 11.

The Archimedes force and intergranular stress for the two types are close, since they are not directly dependent on particle size. The particle-hindrance forces acting the two types of particles are equal in magnitude but opposite in sign, and they reduce the velocity differences between the two

TABLE VI. Input conditions of particle size and density.

		Diameter (d_s) [μm]	Density (ρ_s) [kg/m^3]
Case I	Particle I	80	1000
	Particle II	80	1500
Case II	Particle I	80	1000
	Particle II	80	3000

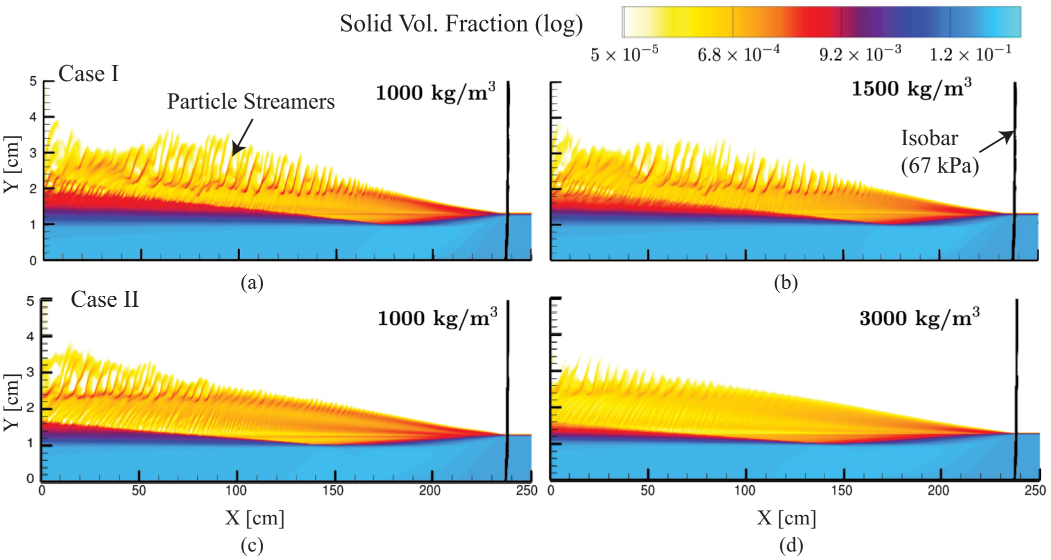

(a) (b)

(c) (d)

FIG. 9. Computed particle volume fractions for both particle types in cases I and II. (a) Particle I in case I ($\rho_s = 1000\ \mathrm{kg/m^3}$); (b) particle II in case I ($\rho_s = 1500\ \mathrm{kg/m^3}$); (c) particle I in case II ($\rho_s = 1000\ \mathrm{kg/m^3}$); and (d) particle II in case II ($\rho_s = 3000\ \mathrm{kg/m^3}$).

particle types. Similar to the 1D results, the drag forces for the two particle types are quite different. Smaller particles experience a larger drag. In the 2D simulations, the lifting force also plays a role since it is proportional to the velocity difference along horizontal direction [see Eq. (50)]. Larger particles that are accelerated more slowly along the gas flow direction will result in a larger velocity

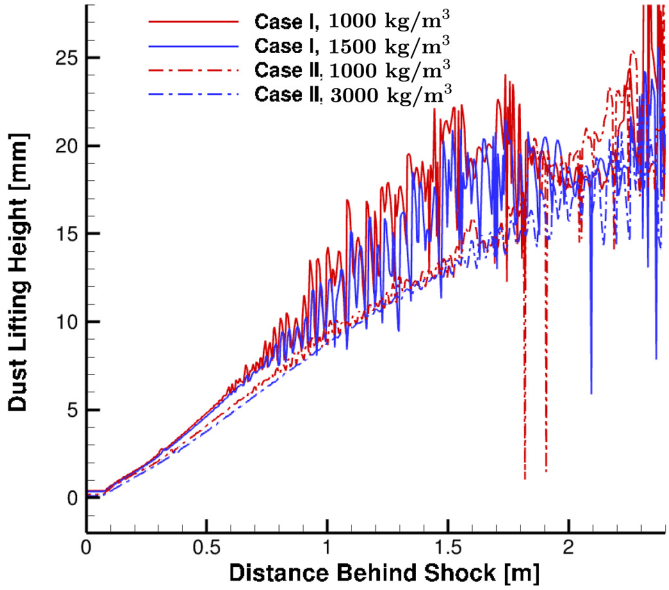

FIG. 10. Computed dust-lifting height for different particle densities. The edge of the dust layer is defined as $\alpha_s = 5 \times 10^{-5}$.

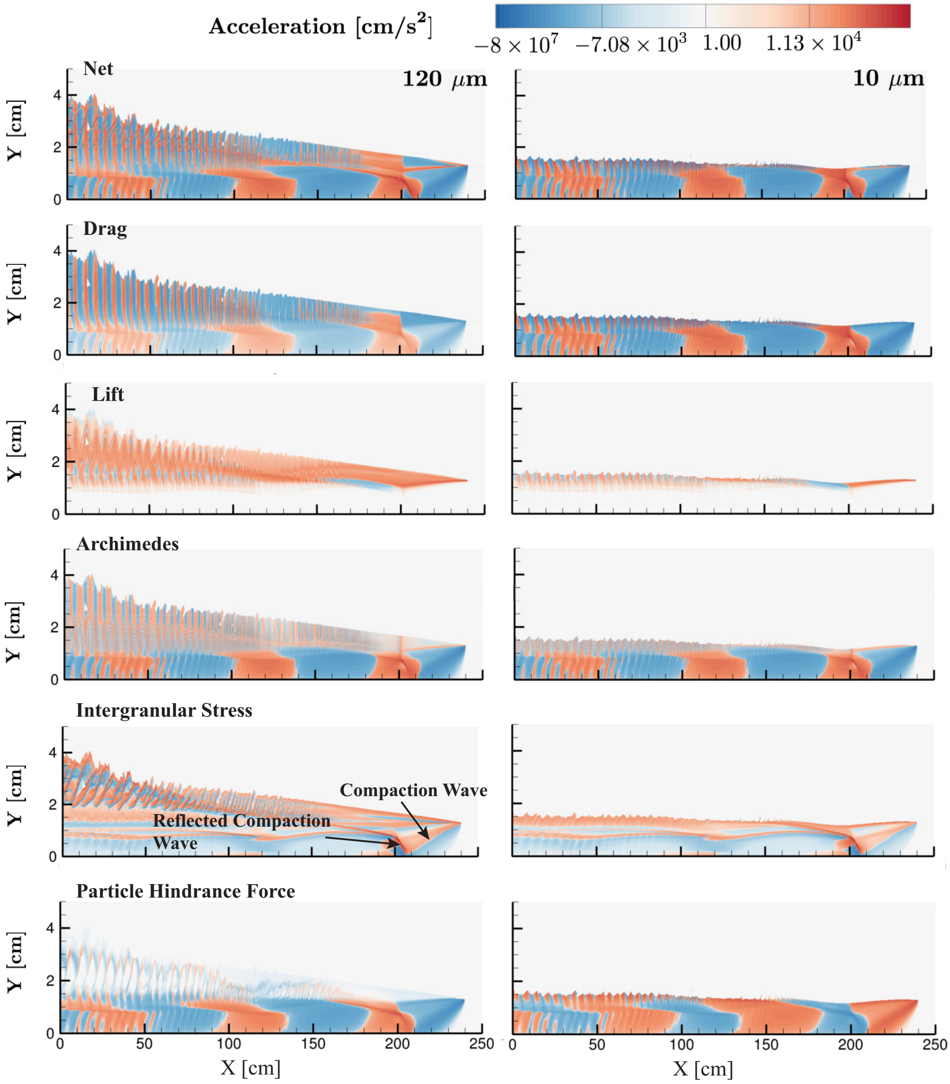

FIG. 11. Net accelerations and accelerations due to drag, lift, Archimedes force, intergranular stress, and particle-hindrance force for both particle types ($d_{s1} = 120\ \mu$m, $d_{s2} = 10\ \mu$m, $\rho_{s1} = \rho_{s2} = 1300\ \mathrm{kg/m^3}$) along vertical direction. Forces have been normalized by $\alpha_s \rho_s$.

difference between the particle and gas phase along horizontal direction. This in turn will result in a larger lift force normal to a boundary layer.

According to Ugarte *et al.* [6], the physical processes occurring near the shock front are the most important for dust lifting. The top left portion of Fig. 12 shows particle-acceleration contours in the region between 150 and 250 cm. The bottom portion of Fig. 12 shows the vertical profiles of particle accelerations due to drag, lift, Archimedes force, intergranular stress, and particle-hindrance force. These profiles are shown for the locations indicated by the three arrows on the contours.

Along line A, which is close to the shock front, the drag and Archimedes forces accelerate particles downward (negative y direction), while the lift force and intergranular stress pull the particles upward (positive y direction). As discussed previously in the one-dimensional simulations, smaller particles experience a larger drag force. Therefore, greater acceleration due to the drag force is pushing

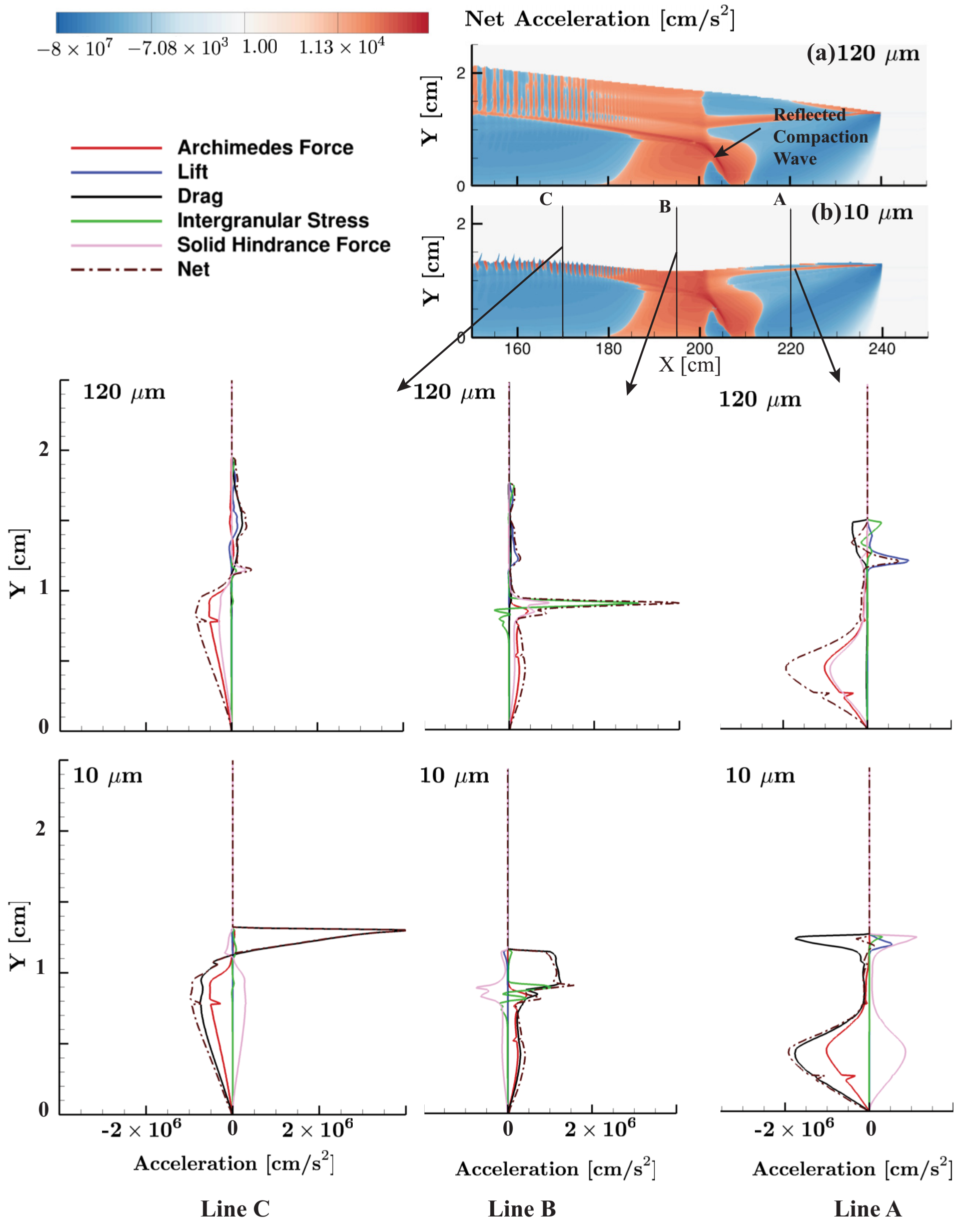

FIG. 12. Vertical accelerations produced by drag, lift, Archimedes force, intergranular stress, and particle-hindrance force along three vertical lines indicated in the net acceleration color map for (a) $d_{s,1} = 120\,\mu$m and (b) $d_{s,2} = 10\,\mu$m. Forces have been normalized by $\alpha_s \rho_s$.

the smaller particles ($ds = 10\,\mu$m) downward. In addition, greater lift force is pulling the larger ($ds = 120\,\mu$m) particles upward in the dispersed region.

Line B is located behind the reflected compaction wave, where a positive net acceleration is produced for both particle types in the dust layer (between 180 and 210 cm). The type II particles are slightly lifted in regions downstream of 190 cm due to this positive acceleration. However, the lifting process is soon overcome through the compaction process (negative acceleration) that dominates in regions to the left of 180 cm.

Line C is located even further behind the shock wave, where there is a negative acceleration in the dust layer and an alternating positive and negative acceleration in the dispersed region. In this region, lift becomes less important and drag dominates. Larger acceleration due to drag is pushing the particles downward in the dust layer for particle type II ($ds = 10\,\mu$m). Although there is a large positive drag force above 1.2 cm along line C for particle type II, the net acceleration (see lower color map) is highly oscillatory and the average value is low.

B. Effect of density

Density is another important aspect affecting dust dispersion. Similar to the 1D result, the 2D simulations shown in Figs. 9 and 10 suggest that heavier particles are lifted slightly lower than lighter particles. Larger particles have a greater inertia and will experience a smaller acceleration given the same net force. In general, heavier particles require a longer responding time to the gas-phase condition.

In addition, the dust layer in the 2D simulations have a relatively high particle volume fraction ($\alpha_{s,1} = \alpha_{s,2} = 0.235$), and the particle-hindrance effect plays an important role in reducing the velocity difference between the two types of particles. Comparing the particle densities in both cases, the heavier particles in case I have a density of 1500 kg/m^3, and the heavier particles in case II have a even greater density (3000 kg/m^3). Therefore, the 3000-kg/m^3 particles are lifted lower than the 1500-kg/m^3 particles since they have a greater inertia. Meanwhile, the heavier particles in both cases exert a particle-hindrance force on the lighter particles (1000 kg/m^3) that is pulling the lighter particles downward. The 3000-kg/m^3 particles, which have the greatest inertia and are lifted to the lowest height, produces a higher particle-hindrance force than the 1500-kg/m^3 particles. This particle-hindrance effect explains why type I particles (1000 kg/m^3) are lifted higher in case I than in case II, even though the size and density of particle type I remain unchanged.

C. Effect of grid refinement

Numerical resolution tests have been performed with three, four, and five levels of refinement, corresponding to the minimum computational cell sizes of 625, 312.5, and 156.3 μm. The computed dust-lifting heights of a shock passing over a dust layer containing two uniformly mixed particle types are shown in Fig. 13. The gas shock is located at 2.2 m and is moving from the left to the right. In these tests, the initial dust-layer height was decreased from 1.27 to 1.25 cm so that all three test cases can have an identical layer thickness.

These tests show reasonable convergence for the small 10-μm particles. For the larger particles, the results show reasonable convergence in the region starting at the shock wave extending back about 1 m. In the region beyond 1 m, the mean values are roughly converged, but the fluctuations in the solution increase with increasing resolution. The increasing fluctuation is related to the formation of "particle streamers" in the dilute dispersed region shown in Fig. 9. These particle streamers are known to not converge under grid refinement using Eulerian-Eulerian methods [32]. Resolving this issue will likely require extending methods to include more advanced models of particle interactions, such as a quadrature-based moment technique [33], which allows particle trajectories to cross. This type of model development is beyond the scope of this paper.

D. Sensitivity of results to model assumptions

There are number of important assumptions that have been made to arrive at the Eulerian model used in this paper. Here we will discussion some of the most important tests that illustrate the validity of these.

The model used in this work neglects terms, such as viscous stresses, granular energy exchange between different types of particles, and dissipation of PTE due to collisions between particles of different types, that are in the complete theory. We recognize that for very dilute flow in one dimension, these terms are negligible because of the low solids volume fraction. This is not true for the two-dimensional case where the particle volume fraction is high. In general, viscous stresses,

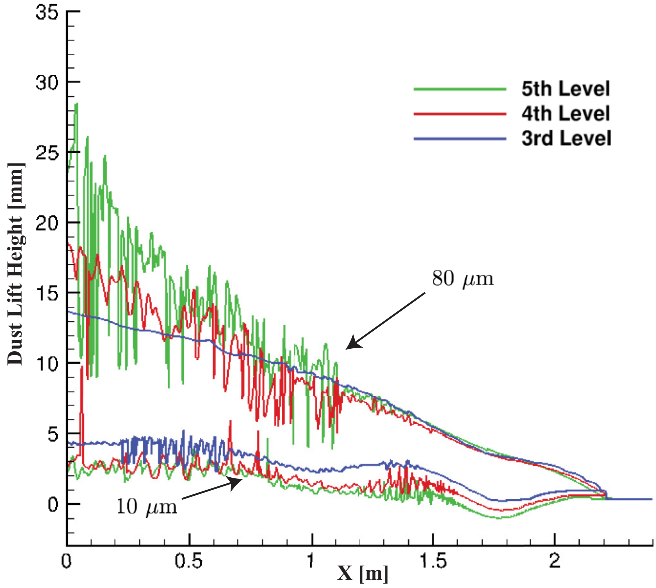

FIG. 13. Computed dust-lifting height of a shock passing over a layer of dust containing two uniformly mixed particle types with three, four, and five levels of refinement ($\rho_{s1} = \rho_{s2} = 1300$ kg/m^3; $d_{s1} = 10\,\mu$m; $d_{s2} = 80\,\mu$m). The edge of the dust layer is defined as $\alpha_s = 5 \times 10^{-5}$.

granular energy exchange between bins, and dissipation of PTE due to collisions between bins are neglected because tests we have done have shown that including these terms does not produce any significant effects on the dust dispersion height, which is our major concern in this study.

1. PTE terms

To validate our assumption of neglecting the granular energy exchange and the dissipation of PTE due to inelastic collisions between different particle bins, simulations with the granular temperatures turned off ($\theta_l = \theta_m = 0$) are performed and compared with the results shown in the paper. By doing this, we are comparing the limiting case, where there is no granular energy for the system, to our current results where the granular energy is slightly higher than the expected value (since we neglected the dissipations due to inelastic collisions between different bins). Figure 14 compares the edge of the dust layer ($\alpha_s = 5 \times 10^{-5}$) assuming zero granular temperature with the results of our current model.

The above figure indicates that the dust is lifted lower for the case with zero granular temperatures, since the solids pressure is eliminated. The difference is more obvious for the case shown on the left ($d_{s1} = 120\ \mu$m, $d_{s2} = 10\ \mu$m) and in regions close to the gas shock. In general, the difference between our current results and the zero-temperature results is insignificant, and the overall trend of the dust dispersion remains unchanged.

Including the dissipation term between different bins would give us a result that falls between the result in the paper and the zero-temperature result. Nevertheless, obtaining the correct amount of energy dissipation and PTE exchange between different bins can be important to our future study, and including these terms is part of our future work.

2. Viscous stresses

In addition, the granular viscous stress terms are neglected in our model. In our research, the major problem of interest is the dispersion height of the dust layer. The densely packed region, where the collisional and friction viscosity plays a more important role, is less important to us here than the

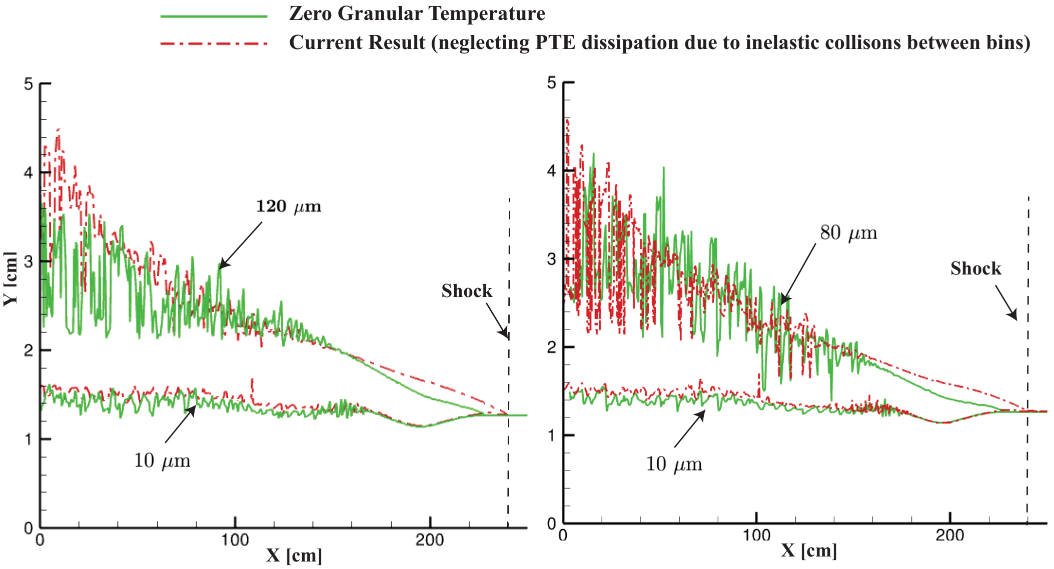

FIG. 14. Comparison of dust-lifting height for cases with zero granular temperatures (solid line) and cases using current model (dashed line). Left: case I ($d_{s1} = 120\ \mu$m, $d_{s2} = 10\ \mu$m); right: case II ($d_{s1} = 80\ \mu$m, $d_{s2} = 10\ \mu$m).

dispersed region. In a similar simulation, Ugarte *et al.* showed that the height of the dispersed dust is in close agreement with the experimental data when granular viscosity terms was ignored [6]. Based on these arguments and for simplicity, the viscosity terms are currently neglected in our simulations. The effect of including the viscosity on dust dispersion is a topic worthy of future study.

3. *Collisional pressure, P_c*

The solids pressure model in Eq. (35) is an approximation. Simulations have been performed with the collisional component $P_{c,lm}$ turned off to test the sensitivity of our result to the model used for $P_{c,lm}$. The results were compared with the those of the current model in Fig. 15. These indicate that turning off the collisional component of the solids pressure produces only slight changes to the particle volume fraction.

4. *Frictional pressure, P_{fric}*

The frictional pressure model in Eq. (43) is developed by Johnson and Jackson [22]. There are a number of other expressions for the friction-collisional pressure available (Koo and Kuo [34], Markatos and Kirkcaldy [35], Nussbaum *et al.* [36], etc.). The expression in Eq. (43) is chosen because it only depends on the particle volume fractions (α_s) and is simple to implement. Houim and Oran showed that the computed results using this expression match closely with the experimental measurements in dense regions [13]. To test the sensitivity of our model to the frictional pressure model used, a simulation with $2 \times P_{\text{fric},l}$ is performed. The results with double P_{fric} and the results using the current model are compared in Fig. 16. These suggest that the particles with double frictional pressure become slightly less compacted and are lifted to a higher level. The difference is, however, negligible.

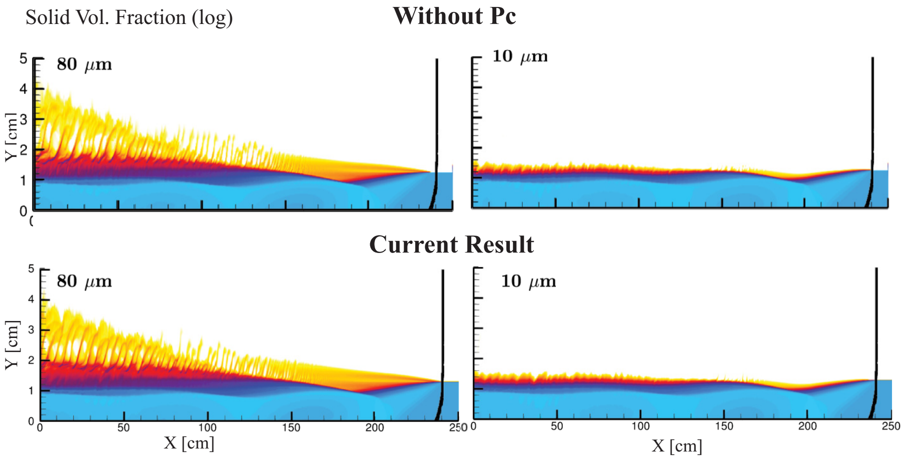

FIG. 15. Particle volume fraction of a shock passing over a dust layer containing two types of particles ($d_{s1} = 80\ \mu$m, $d_{s2} = 10\ \mu$m). Top: simulation results assuming zero collisional pressure ($P_{c,lm} = 0$); bottom: results with current model.

VIII. SUMMARY AND CONCLUSIONS

This paper presents one- and two-dimensional numerical simulations of a shock interacting with a granular mixture containing multiple particle types. The granular model used here takes into accounts multiple particle types with a binning approach. Each bin of particles has its own characteristic uniform particle size and density. Solving the equations for a granular mixture containing one gas phase and M particle types involves solving ($M + 1$) unsteady, multidimensional sets of conservation equations. Equations for each bin of particles are coupled with the gas flow as well as all other particle types.

One-dimensional simulations of a Mach-1.4 shock passing through a dilute particle curtain containing two uniformly mixed particles types are performed. In addition, two-dimensional

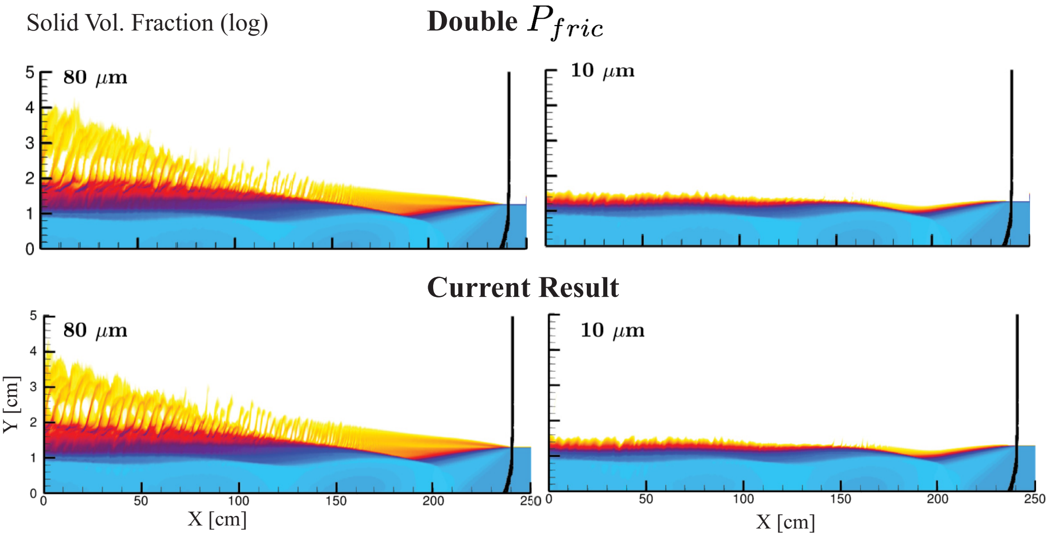

FIG. 16. Particle volume fraction of a shock passing over a dust layer containing two types of particles ($d_{s1} = 80\ \mu$m, $d_{s2} = 10\ \mu$m). Top: simulation results with $2 \times P_{\text{fric},l}$; bottom: results with current model ($1 \times P_{\text{fric},l}$).

simulations of a shock passing over a dust layer containing two particles types are performed. Particle sizes and densities are selected to investigate the effect of particle size and density separately.

The 1D results indicate that particles with different sizes or densities behave differently under the same background gas-flow conditions and they can separate into different clouds even though they were initially uniformly mixed with each other. Particles with larger inertia require a longer relaxation time to the postshock condition and therefore are accelerated more slowly.

The 2D results for a shock passing over a dust layer shows that larger particles are lifted higher than smaller particles, while lighter particles are lifted higher than heavier particles. Larger particles near the shock experience a smaller drag force pushing the particles into the dust layer and a smaller lifting force pulling the particle out of the dust layer. Particle size plays a significant role on dust dispersion behind a moving shock, while particle density only has a minor effect.

ACKNOWLEDGMENTS

This work was supported in part by NIOSH Grant No. 200-2015-64091 and in part by the University of Maryland through Minta Martin Endowment Funds in the Department of Aerospace Engineering and through the Glenn L. Martin Institute Chaired Professorship at the A. James Clark School of Engineering. The authors would like to thank Mike Spako and Marcia Harris for their valuable comments and suggestions. We also thank the two anonymous reviewers for providing helpful comments on the earlier drafts of the manuscript. The authors acknowledge the University of Maryland supercomputing resources (http://www.glue.umd.edu/hpcc) made available in conducting the research reported in this paper.

[1] B. Fletcher, The interaction of a shock with a dust deposit, J. Phys. D **9**, 197 (1976).

[2] C. C. Hwang, Initial stages of the interaction of a shock wave with a dust deposit, Int. J. Multiphase Flow **12**, 655 (1986).

[3] A. R. Pinkus and V. M. Parisi, Helicopter brown-out landing, U.S. Patent No. 7,642,929 (2010).

[4] C. J. Cawthorn, Several applications of a model for dense granular flows, Ph.D. thesis, University of Cambridge, Cambridge, UK, 2011.

[5] C. K. Man and K. A. Teacoach, How does limestone rock dust prevent coal dust explosions in coal mines? Mining Engineering **61**, 69 (2009).

[6] O. J. Ugarte, R. W. Houim, and E. S. Oran, Examination of the forces controlling dust dispersion by shock waves, Phys. Rev. Fluids **2**, 074304 (2017).

[7] T. Suzuki and T. Adachi, The effects of particle size on shock wave-dust deposit interaction, in *Proceedings of the 14th International Symposium on Space Technology and Science* (AGNE Publishing, Inc, Tokyo, Japan, 1984), pp. 483–490.

[8] C. J. Zhu, B. Q. Lin, B. Y. Jiang, Q. Liu, and Y.-D. Hong, Dust lifting behind a shock wave: Analysis based on the ee method, Journal of China University of Mining and Technology **41**, 733 (2012).

[9] W. Boyi, X. Yi, C. Qian, and A. N. Osiptsov, Dust-cloud structures behind a shock wave moving over a deposited layer of fine particles, Prog. Nat. Sci. **15**, 972 (2005).

[10] A. Y. Chowdhury, Shock interaction with dust layers, Ph.D. thesis, Texas A&M University, College Station, 2015.

[11] A. Rosato, K. J. Strandburg, F. Prinz, and R. H. Swendsen, Why the brazil nuts are on top: Size segregation of particulate matter by shaking, Phys. Rev. Lett. **58**, 1038 (1987).

[12] Beckman Coulter, Ls 13 320 laser diffraction particle size analyzer: Instructions for use [https://www.beckmancoulter.com/wsrportal/techdocs].

[13] R. W. Houim and E. S. Oran, A multiphase model for compressible granular-gaseous flows: Formulation and initial tests, J. Fluid Mech. **789**, 166 (2016).

[14] D. J. Gunn, Transfer of heat or mass to particles in fixed and fluidised beds, Int. J. Heat Mass Transf. **21**, 467 (1978).

[15] D. Gidaspow, *Multiphase Flow and Fluidization: Continuum and Kinetic Theory Descriptions* (Academic Press, San Diego, CA, 1994).

[16] D. L. Koch and A. S. Sangani, Particle pressure and marginal stability limits for a homogeneous monodisperse gas-fluidized bed: Kinetic theory and numerical simulations, J. Fluid Mech. **400**, 229 (1999).

[17] C. K. K. Lun, S. B. Savage, D. J. Jeffrey, and N. Chepurniy, Kinetic theories for granular flow: Inelastic particles in Couette flow and slightly inelastic particles in a general flowfield, J. Fluid Mech. **140**, 223 (1984).

[18] M. Syamlal, W. Rogers, and T. J. O'Brien, MFIX documentation theory guide, National Energy Technology Laboratory, Department of Energy, Technical Notes DOE/METC-95/1013 and NTIS/DE95000031, 1993 (unpublished).

[19] S. Benyahia, M. Syamlal, and T. J. O'Brien, Summary of MFIX equations 2012-1 [https://mfix.netl.doe.gov/documentation/MFIXEquations2012-1.pdf].

[20] A. B. Yu and N. Standish, Porosity calculations of multi-component mixtures of spherical particles, Powder Technol. **52**, 233 (1987).

[21] L. Huilin, H. Yurong, and D. Gidaspow, Hydrodynamic modeling of binary mixture in a gas bubbling fluidized bed using the kinetic theory of granular flow, Chem. Eng. Sci. **58**, 1197 (2003).

[22] P. C. Johnson and R. Jackson, Frictional-collisional constitutive relations for granular materials, with application to plane shearing, J. Fluid Mech. **176**, 67 (1987).

[23] Y. H. Yu and C.-Y. Wen, Mechanics of fluidization, *Chemical Engineering Progress Symposium Series* (American Institute of Chemical Engineers, New York, 1966), Vol. 62, p. 100.

[24] S. Ergun, Fluid flow through packed columns, *Chemical Engineering Progress Symposium Series* (American Institute of Chemical Engineers, New York, 1952), Vol. 48, p. 89.

[25] D. A. Drew and R. T. Lahey, The virtual mass and lift force on a sphere in rotating and straining inviscid flow, Int. J. Multiphase Flow **13**, 113 (1987).

[26] M. Syamlal, The particle-particle drag term in a multiparticle model of fluidization, Tech. Rep., EG and G Washington Analytical Services Center, Inc., Morgantown, WV, 1987 (unpublished).

[27] R. W. Houim and K. K. Kuo, A low-dissipation and time-accurate method for compressible multi-component flow with variable specific heat ratios, J. Comput. Phys. **230**, 8527 (2011).

[28] M. Pelanti and R. J. LeVeque, High-resolution finite volume methods for dusty gas jets and plumes, SIAM J. Sci. Comput. **28**, 1335 (2006).

[29] R. J. Spiteri and S. J. Ruuth, A new class of optimal high-order strong-stability-preserving time discretization methods, SIAM J. Numer. Anal. **40**, 469 (2002).

[30] J. Bell, A. Almgren, V. Beckner, M. Day, M. Lijewski, A. Nonaka, and W. Zhang, Boxlib user's guide, Technical Report CCSE Lawrence Berkeley National Laboratory, 2012.

[31] A. Y. Chowdhury, H. G. Johnston, B. Marks, M. S. Mannan, and E. L. Petersen, Effect of shock strength on dust entrainment behind a moving shock wave, J. Loss Prevent. Process Ind. **36**, 203 (2015).

[32] E. Helland, R. Occelli, and L. Tadrist, Numerical study of cluster formation in a gas-particle circulating fluidized bed, Powder Technol. **110**, 210 (2000).

[33] O. Desjardins, R. O. Fox, and P. Villedieu, A quadrature-based moment method for dilute fluid-particle flows, J. Comput. Phys. **227**, 2514 (2008).

[34] J. H. Koo and K. K. Kuo, Transient combustion in granular propellant beds. Part I. Theoretical modeling and numerical solution of transient combustion processes in mobile granular propellant beds, Tech. Rep., Pennsylvania State University, University Park Department of Mechanical Engineering, 1977 (unpublished).

[35] N. C. Markatos and D. Kirkcaldy, Analysis and computation of three-dimensional, transient flow and combustion through granulated propellants, Int. J. Heat Mass Transf. **26**, 1037 (1983).

[36] J. Nussbaum, P. Helluy, J.-M. Hérard, and A. Carriere, Numerical simulations of gas-particle flows with combustion, Flow, Turbul. Combust. **76**, 403 (2006).

Correction: Another affiliation has been added for the second author.